

Transition to collapsed tetragonal phase in CaFe_2As_2 single crystals as seen by ^{57}Fe Mössbauer spectroscopy

Sergey L. Bud'ko,¹ Xiaoming Ma,^{1,2} Milan Tomić,³

Sheng Ran,^{1,*} Roser Valentí,³ and Paul C. Canfield¹

¹*Ames Laboratory, US DOE and Department of Physics and Astronomy,*

Iowa State University, Ames, Iowa 50011, USA

²*Institute of Applied Magnetism, Key Laboratory for Magnetism*

and Magnetic Materials of the Ministry of Education,

Lanzhou University, Lanzhou 730000, Gansu Province, China

³*Institut für Theoretische Physik, Goethe-Universität Frankfurt,*

Max-von-Laue-Straße 1, 60438 Frankfurt am Main, Germany

(Dated: March 2, 2024)

Abstract

Temperature dependent measurements of ^{57}Fe Mössbauer spectra on CaFe_2As_2 single crystals in the tetragonal and collapsed tetragonal phases are reported. Clear features in the temperature dependencies of the isomer shift, relative spectra area and quadrupole splitting are observed at the transition from the tetragonal to the collapsed tetragonal phase. From the temperature dependent isomer shift and spectral area data, an average stiffening of the phonon modes in the collapsed tetragonal phase is inferred. The quadrupole splitting increases by $\sim 25\%$ on cooling from room temperature to ~ 100 K in the tetragonal phase and is only weakly temperature dependent at low temperatures in the collapsed tetragonal phase, in agreement with the anisotropic thermal expansion in this material. In order to gain microscopic insight about these measurements we perform *ab initio* density functional theory calculations of the electric field gradient and the electron density of CaFe_2As_2 in both phases. By comparing the experimental data with the calculations we are able to fully characterize the crystal structure of the samples in the collapsed-tetragonal phase through determination of the As z -coordinate. Based on the obtained temperature dependent structural data we are able to propose charge saturation of the Fe - As bond region as the mechanism behind the stabilization of the collapsed-tetragonal phase at ambient pressure.

I. INTRODUCTION

CaFe₂As₂ is conceivably one of the most interesting materials in the family of Fe-As based superconductors with a very fragile ground state and extreme sensitivity to the external pressure and/or strain. At ambient pressure, a clear, sharp, first order transition at ~ 170 K from high temperature tetragonal - paramagnetic phase to low temperature orthorhombic - antiferromagnetic phase was observed in thermodynamic, transport and microscopic measurements, in single crystals grown out of Sn flux.¹⁻⁶ Under pressure, this transition is initially suppressed at a rate of 10-15 K/kbar^{5,7-11}. As the pressure increases, at about 3 kbar, a paramagnetic - collapsed tetragonal (cT) phase terminates the lower pressure orthorhombic - antiferromagnetic phase near 100 K. The cT transition temperature increases under pressure and reaches 300 K at ~ 15 kbar.⁷⁻⁹ The uniaxial pressure derivatives of the structural/magnetic transition are large and of different signs.¹² The pressure - temperature phase diagram for CaFe₂As₂ is very sensitive to non-hydrostaticity of the applied pressure.^{5,10,13,14}

This extreme sensitivity of pure, as well as substituted CaFe₂As₂ single crystals to external stresses and strains yields an unexpected result: by a judicious choice of the annealing temperature and time (e.g. by control of internal stress fields via nanoscale precipitates) we can tune the structural/magnetic transition temperature in FeAs grown CaFe₂As₂ crystals in a manner similar to application of pressure: suppressing the antiferromagnetic/orthorhombic transition by over 70 K and furthermore, we can obtain the crystals with the cT ground state at ambient pressure.¹⁵ By adding transition metal substitution as an extra parameter, we can tune the ground state of the Ca(Fe_{1-x}T_x)₂As₂ (T = Co, Ni, Rh) crystals to be orthorhombic - antiferromagnetic, tetragonal - superconducting, tetragonal - paramagnetic, and collapsed tetragonal - paramagnetic, all at ambient pressure.^{16,17} Pressure measurements on Co-substituted CaFe₂As₂ further illustrate the similar effects of applied pressure and post - growth annealing and quenching of samples¹⁸ and also underscore the system's pressure sensitivity with $dT_{(AFM/ortho)}/dP \approx -110$ K/kbar and $dT_c/dP \approx -6$ K/kbar.

The aforementioned tunability of CaFe₂As₂ created the opportunity for studies of the cT phase at ambient pressure (e.g. in FeAs grown CaFe₂As₂ single crystals quenched from 960° C), using experimental techniques that are either difficult or impossible to combine with hydrostatic pressure.¹⁹⁻²⁴

^{57}Fe Mössbauer spectroscopy has been widely used to study Fe-As based superconductors and related materials,^{25–29} including Sn-grown CaFe_2As_2 single crystals^{6,30,31} and powdered single crystals³² primarily for probing magnetism (although it should be noted that grinding of CaFe_2As_2 affects the macroscopic and microscopic magnetic properties³³). In this work we will use this local probe technique to perform a detailed temperature-dependent study of the cT transition (and the cT phase) in single crystals of undoped, FeAs-grown 960°C quenched¹⁵, CaFe_2As_2 . In these CaFe_2As_2 samples both the high temperature tetragonal and low temperature cT phases are paramagnetic, with no magnetic order. We will compare the results with the available literature data on temperature and pressure induced transition to the cT phase. Some initial ^{57}Fe Mössbauer spectroscopy data on very similar FeAs-grown CaFe_2As_2 crystals with cT ground state were published in Ref. 15 and the pressure induced transition to the cT phase at room temperature in Sn-grown sample was recently studied by Mössbauer spectroscopy in Ref. 34.

The isomer shift and the quadrupole splitting observed in Mössbauer spectroscopy can be directly related to the electron density at the nucleus and the electric field gradient respectively, both of which can be calculated in the framework of *ab-initio* Density Functional Theory. We will employ these calculations in order to provide a theoretical interpretation of the measurements, as well as to obtain a full structural characterization of the 960°C quenched samples in the collapsed-tetragonal phase by determining the As z -coordinates. We will also analyze the temperature dependent structural data in order to understand the microscopic mechanism responsible for the stabilization of the collapsed-tetragonal phase at ambient pressure.

II. EXPERIMENTAL DETAILS AND COMPUTATIONAL METHODS

CaFe_2As_2 single crystals were grown from ternary melts rich in FeAs, following the procedure described in Ref. 15. The excess liquid was decanted at 960°C , essentially quenching the samples from 960°C to room temperature. The cT transition temperature of the sample was $\sim 90\text{K}$ as confirmed by dc magnetization measurements (see Fig. 1).¹⁵ In the rest of the paper we will use CaFe_2As_2 to refer to these FeAs grown, CaFe_2As_2 samples quenched from 960°C to room temperature.

Mössbauer spectroscopy measurements were performed using a SEE Co. conventional,

constant acceleration type spectrometer in transmission geometry with a $^{57}\text{Co}(\text{Rh})$ source kept at room temperature. The absorber was prepared as a mosaic of 0.04 - 0.1 mm thick single crystals held between two paper disks by a small amount of a pressure sensitive adhesive. The gaps between the individual crystals were kept as small as possible. The mosaic had the c - axis perpendicular to the disks (with the accuracy of or better than $\pm 10^\circ$) and arbitrary in-plane orientation. Since CaFe_2As_2 and related materials are known to be very sensitive to the stresses and strains, including those caused by sample mounting,³⁵ we performed dc magnetization measurements on a subset of the mosaic with the same mounting as for the Mössbauer measurements (Fig. 1). The cT transition is still sharp, without apparent shift of the transition temperature.

The constraints on the thickness of the CaFe_2As_2 crystals that can be cleaved without significant mechanical damage result in the absorber having 5-20 mg natural Fe per cm^2 that corresponds to a "thick" absorber limit.³⁶ The consequences of using "thick" absorber include thickness broadening of the absorption lines, increased error bars in absolute determination of the quadrupole splitting and different degrees of saturation of the absorption lines of different intensity. The intrinsic linewidth found in inorganic compounds is often in the range of 0.26 - 0.28 mm/s,³⁶ so the broadening observed in our measurements is not extremely severe. The other effects of the absorber thickness manifest as "smooth" contribution to the temperature dependent data and cannot cause the sharp features observed in the temperature dependences of the hyperfine parameters at the cT transition.

The absorber holder consists of two nested white Delrin cups. The absorber holder was locked into thermal contact with a copper block with a temperature sensor and a heater, and was aligned with the γ - source and detector. The c -axis of the crystals in the mosaic was parallel to the Mössbauer γ beam. The absorber was cooled to a desired temperature using a Janis model SHI-850-5 closed cycle refrigerator (with vibration damping). The measurements were performed on warming, after initially cooling the absorber down to a base temperature of 4.6 K. The driver velocity was calibrated using an α -Fe foil and all isomer shifts (IS) are quoted relative to the α -Fe foil at room temperature. All the Mössbauer spectra were fitted by the commercial software package MossWinn.³⁷

Ab initio Density Functional Theory (DFT) calculations were performed with the scalar relativistic Full Potential Local Orbital method (FPLO)³⁸. The electric field gradients were obtained according to the technique described in Ref. 39 and implemented in the FPLO

code. The Perdew-Burke-Erzenhof⁴⁰ exchange-correlation potential was employed for all calculations, and we considered $20 \times 20 \times 20$ k-point meshes, with charge density converged within 10^{-8} a.u.⁻³. In order to calculate the electron density at the location of atomic nuclei, we assumed the model of a finite-size nucleus with constant charge density. Consistency of the calculated electric field gradients and electron densities was verified against values obtained by the Full-Potential Linearized Augmented Plane-Wave method implemented in the WIEN2K code⁴¹.

III. EXPERIMENTAL RESULTS AND DISCUSSION

The ⁵⁷Fe Mössbauer spectra of CaFe₂As₂ at selected temperatures between the room temperature and the base temperature of 4.6 K are shown in Fig. 2. At each temperature the spectrum is a quadrupole split doublet with the higher velocity line having almost twice the intensity of the lower velocity line. No secondary phase signal was observed in the spectra. Visually, the temperature induced changes, even near $T_{cT} \sim 90$ K, are subtle.

The temperature dependent linewidth of the spectra is shown in Fig. 3 a). Overall the linewidth increases by a few percent on cooling from room temperature to the base temperature. As has been discussed in Ref. 15, the point symmetry and the location of the Fe site in the ThCr₂Si₂ structure constrains the principal axis of the local electric field gradient tensor to the *c* - crystalline axis, as a result, a doublet lines intensity ratio of 3 : 1 is expected for the mosaic with the *c* - axis parallel to the γ beam. Instead, the observed room temperature ratio is $\sim 2.4 : 1$ and it decreases to $\sim 1.95 : 1$ at the base temperature (Fig. 3 (b)). The general behavior is consistent with the two temperature points reported earlier.¹⁵ Several possible reasons for the doublet lines intensity ratio being different from 3 : 1 were discussed in Ref. 15. Most probably, an intensity ratio smaller than 3 : 1 and its further decrease on cooling may be due to the "thick" absorber conditions of the measurements (consistent with the large absorption observed (Fig. 2)). We observe a small but distinct feature in the intensity ratio at the transition temperature around ~ 90 K. The change in the intensity ratio at the cT transition reflects an increase of the degree of saturation (caused by the thick absorber) of the stronger spectral line, thus pointing to stiffening of the lattice in the low temperature cT phase.

In Fig. 4 we show the measured isomer shift (IS) which increases upon cooling and has

a clear step-like change between 95 K and 85 K. The isomer shift includes contributions from both the chemical shift and the second-order Doppler shift. The latter is known to increase convexly upon decreasing temperature, due to gradual depopulation of the excited phonon states. However, it should be constant at low temperature, because of the quantum mechanical zero-point motion. The chemical shift should not depend on temperature. The main contribution to the temperature dependence of the isomer shift is therefore from the second-order Doppler shift, and is usually described by the Debye model:^{36,42}

$$\delta(T) = \delta(0) - \frac{9 k_B T}{2 M c} \left(\frac{T}{\Theta_D} \right)^3 \int_0^{\Theta_D/T} \frac{x^3 dx}{e^x - 1}, \quad (1)$$

where c is the velocity of light, M is the mass of the ^{57}Fe nucleus, and $\delta(0)$ is the temperature-independent part. For the isomer shift data in Fig. 4 separate Debye fits, for the tetragonal phase ($T \geq 95$ K) and for the collapsed tetragonal phase ($T \leq 85$ K) were performed. The fits yield $\Theta_D = 239 \pm 16$ K for the high temperature tetragonal phase and $\Theta_D = 316 \pm 7$ K for the low temperature cT phase. These results suggest that the lattice is stiffer in the cT phase. It has to be noted that the results of the fit in the low temperature cT phase should be taken with caution, since the fit is performed on a limited dataset with only minor temperature dependence. Still the conclusions are consistent with the rest of the data discussed in this work.

The relative spectral area (Fig. 5) also shows a distinct step - like feature in the region of the structural transition. Although we do not perform a Debye fit of the temperature dependent spectral area due to the possible effects of the thick absorber, the step - like increase of spectral area (by $\sim 6\%$) at the cT transition points to an increase of the Debye temperature, i.e. stiffening of the lattice, in the cT phase. Somewhat higher, $\sim 9\%$, increase in the relative spectral area is expected using Θ_D values from fits of temperature-dependent isomer shift and the Debye model for the recoil-free fraction:^{36,42}

$$f = \exp \left\{ \frac{-3E_\gamma^2}{k_B \Theta_D M c^2} \left[\frac{1}{4} + \left(\frac{T}{\Theta_D} \right)^2 \int_0^{\Theta_D/T} \frac{x dx}{e^x - 1} \right] \right\}, \quad (2)$$

(where f is the recoil-free fraction, and E_γ is the γ -ray energy) leading to the conclusion that the value of Θ_D in the cT phase may be slightly overestimated.

Stiffening of the lattice upon transition to a collapsed tetragonal phase (under pressure) was clearly observed in BaFe_2As_2 ⁴³ via compressibility measurements, however similar sets^{9,43} of structural data for CaFe_2As_2 appear to be less convincing. Nonetheless, a detailed study of phonon spectra in CaFe_2As_2 ⁴⁴ concluded that the phonons polarized in the ab plane are very similar in the tetragonal and cT phases, whereas transverse acoustic phonons propagating along the c direction stiffen very significantly in the cT phase. These results are consistent with our analysis of the changes in the Mössbauer spectra at the structural transition.

The temperature dependent quadrupole splitting (QS) data is presented in Fig. 6. The total change of the QS with temperature is $\sim 25\%$. QS varies strongly in the tetragonal phase and is almost constant in the cT phase. The cT transition is clearly seen as a cusp in QS(T). Qualitatively, this behavior is consistent with the anisotropic thermal expansion of CaFe_2As_2 ²¹: the quadrupole splitting is related to the c/a ratio, that changes considerably above the cT transition and significantly less in the cT phase. In a very general sense this behavior is consistent with the results from the Ref. 34 (with pressure as a control parameter): QS increases on approaching the cT transition, displays a cusp at the transition, and does not change in a significant manner in the cT phase. The origin of the cusp in the QS(T) data at the cT transition (possibly observed as a function of pressure³⁴ as well) is however not clear and requires additional studies beyond the scope of the present work.

IV. MICROSCOPIC MODELLING

To better understand the physics behind the experimental observations we rely on the fact that the isomer shift and the quadrupole splitting are directly related to the electronic charge densities and the electric field gradients, which can be calculated *ab-initio* in the framework of density functional theory (DFT).

The isomer shift δ can be expressed⁴² as:

$$\delta = \frac{Ze^2}{5\varepsilon_0}(R_e^2 - R_g^2)[\rho_a(0) - \rho_s(0)] \quad (3)$$

where Z is the nuclear charge, e is the elementary charge, ε_0 is the permittivity in vacuum, R_g and R_e are the nuclear ground and excited state radii and $\rho_s(0)$ and $\rho_a(0)$ are electron

densities at the source and absorption nuclei respectively. The only quantity that varies in the measurement is the electron density around the absorption nucleus $\rho_a(0)$ so that we can simply write Eq. (3) as a linear relation

$$\delta = a[\rho_a(0) - b] \quad (4)$$

Note that for ^{57}Fe the constant a is negative^{45–49}. With this taken into account, part of the observed step-like increase in the isomer shift at the onset of the volume collapse (Fig. 4) would correspond to the likewise drop in the electron density at the iron nucleus. This can be explained as an immediate consequence of Fe charge delocalization brought in by the volume collapse as a result of a strong, first order, structural phase transition.

Furthermore, the quadrupole splitting Δ can be expressed as⁴²:

$$\Delta = \frac{1}{2}eQV_{zz}\sqrt{1 + \frac{\eta^2}{3}} \quad (5)$$

where Q is the nuclear quadrupole moment, $\eta = |V_{xx} - V_{yy}|/|V_{zz}|$ is the electric field gradient asymmetry, and $|V_{xx}| \leq |V_{yy}| \leq |V_{zz}|$ are the eigenvalues of the electric field gradient tensor. Since the sample is tetragonal, the asymmetry η is zero and we obtain the following linear equation

$$\Delta = cV_{zz} \quad (6)$$

where $c = eQ/2$.

Understanding the origin of the QS behavior (Fig. 6) based on Eq. 6 is quite involved since the electric field gradient V_{zz} strongly depends on crystal structural details, in particular the details of the Fe-As bonding.

The crystal structure of the tetragonal CaFe_2As_2 is that of ThCr_2Si_2 ⁵⁰ and is described by the space group $I4/mmm$. The Wyckoff positions corresponding to Ca and Fe atoms are fully fixed by the symmetry, while the Wyckoff position corresponding to the As atoms has only x and y coordinates fixed, leaving the z -coordinate as the sole internal structural degree of freedom.

The structure of the 960° C quenched CaFe₂As₂ sample was characterized in the 5-300 K temperature range by X-ray diffraction measurements¹⁵. However, these measurements were able to determine only the unit cell parameters, and the As z -coordinate was left unknown, rendering the crystal structure information incomplete.

Full crystal structure information is the starting point for any DFT calculation. Since we don't have here information of the As z -coordinate but we do have valuable information from experiment on isomer shifts and quadrupole splittings, we are going to perform a “reverse engineering”, namely from the experimental data we will deduce the As z coordinates as a function of temperature. We would like to point out that the task of providing an accurate determination of the As z -coordinates has additional importance through the fact that As atom positions are controlling parameters in the tetrahedral coordination geometry of the Fe atoms (see Fig. 7 b)), and they are thus a very sensitive driver of physics of the iron-arsenide layer⁵¹.

Obtaining the As z -coordinate in a straightforward way, by structural optimization within DFT, may be rather inaccurate because it would require the accurate reproduction of the intricate internal mechanical conditions experienced by the samples used in the experiment. In this particular case, the sample strain, where Sn-grown single crystals are taken as a reference, is substantial enough to maintain the collapsed-tetragonal phase at the ambient pressure, and as a consequence, cannot be ignored in any theoretical description pretending to be an accurate portrayal of reality.

To get around this problem, we chose a different strategy. We exploit the linear relationship between the quadrupole splitting and the electric field gradient (Eq. (6)). The proportionality constant is the electron charge multiplied by the ⁵⁷Fe nuclear quadrupole moment, which is a well determined quantity, with values 0.15-0.17 barn^{48,52-57}. This allows us to compute the quadrupole splitting by calculating V_{zz} . We consider unit cell parameters experimentally determined at temperature T ,¹⁵ calculate the quadrupole splitting Δ_{DFT} for a range of As z -coordinates and then perform a polynomial fit of the calculated data points to obtain a curve $\Delta_{\text{DFT}}(T, z(T))$, where $z(T)$ denotes As z -coordinate at temperature T . We then determine the z -coordinates by solving numerically $\Delta_{\text{DFT}}(T, z(T)) = \Delta_{\text{exp}}(T)$, where $\Delta_{\text{exp}}(T)$ is the quadrupole splitting experimentally determined at temperature T . The As z -coordinates obtained in this way are shown in Fig. 7 along with the height of As atoms above the Fe plane. Although the quadrupole splitting shows non-monotonous behavior

in the 0-90 K region, reversing the decrease around 30 K, the As z -coordinate, and corresponding height above the Fe plane display a monotonous increase and decrease respectively, indicating the well known complex relationship between the position of the As atom and the electronic properties⁵¹.

Since the As z -coordinates now satisfy Eq. (6) by construction, being able to simultaneously satisfy Eq. (4) provides an important consistency check. In Fig. 8 we show the relationship between the measured isomer shift and the electron density calculated for the As z -coordinates obtained from the quadrupole splitting. The data is fitted very well by a linear function and the slope is determined to be $a = -0.45 \pm 0.04$ [a.u.³ mm/s] which is in good agreement with previously reported values for ⁵⁷Fe in various compounds⁴⁶⁻⁴⁹.

It is important to note here that Figs. 7 and 8 are restricted to the collapsed-tetragonal phase, since in the tetragonal phase the experimentally measured values of the quadrupole splittings cannot be reproduced by the calculations within a reasonable range of As z -coordinate values. We attribute this to the fact that antiferromagnetic fluctuations and electronic correlation effects cannot be accurately captured within DFT. In the collapsed tetragonal phase it has been shown that both correlation effects^{22,58,59} and antiferromagnetic fluctuations^{22,60} are suppressed resulting in a good agreement between our DFT calculations and the Mössbauer measurements.

Focusing now on the tetragonal phase, it is well known that matching the experimentally determined and the DFT calculated equilibrium, As z -coordinates in Fe-based superconductors is, in general, problematic as has been pointed out by numerous publications⁶¹⁻⁶⁴. However, spin polarized calculations within GGA have been shown to provide reasonable estimates, specially for the orthorhombic phases with long range magnetic order⁶².

Such approach can be used here to mimic the effect of electron correlation and antiferromagnetic fluctuations in the tetragonal phase in the framework of DFT. We have experimented with spin-polarized GGA calculations with and without on-site Coulomb repulsion. In this way we were able to extract more reasonable estimates for As z -coordinates. Here we present results with $U=3$ eV and Hund's coupling $J=1$ eV. We assume Néel order in order to preserve the tetragonal symmetry and account for the antiferromagnetic character of fluctuations. In this way we obtain an estimate of the As z -coordinate in the tetragonal phase which *should be taken only as an indication of the general temperature trend*. An LDA+DMFT (Local Density Approximation plus Dynamical Mean Field Theory) calcula-

tion would be more appropriate but it is beyond the scope of the present work.

Figure 9 a) shows the DFT predicted Fe-As bond lengths both in the collapsed tetragonal and the tetragonal phase. As the sample is cooled down the Fe-As bond length decreases, driven by thermal contraction. Interestingly, this trend reverses in the collapsed tetragonal phase where the Fe-As bond length increases, working against the thermal contraction of the sample. It is instructive to compare this behavior to the experimentally determined Fe-As bond lengths at ambient pressure and 0.63 GPa in Sn-grown samples subjected to hydrostatic pressure⁸. We would like to stress here that the data shown corresponds to available measurements⁸ for CaFe_2As_2 performed under *different conditions* to those used in the present study and thus our *ab initio* DFT results are not meant to reproduce these data. However, as we will show below, comparison to Sn grown, low strain, samples at $P = 0$ and $P = 0.63$ GPa provides references to help define the expected range of behavior seen in our CaFe_2As_2 sample.

All measurements in our study are performed at ambient pressure and on samples that have a certain amount of strain relative to the Sn-grown samples from Ref. 8. We can thus consider the samples used in our study to be *intrinsically* under certain amount of pressure, even at zero external pressure. Keeping this analogy in mind we can proceed now with the structural comparison. We observe that our predicted bond lengths fit into the experimentally observed range of bond lengths and that, despite the fact that the predicted bond lengths in the tetragonal phase are just a rough estimate, they are consistent with the experimental data when we take into account the differences in experimental conditions. Namely, the hydrostatic pressure stabilizes the cT phase below 200 K at 0.63 GPa in Sn-grown samples, while in our 960° C quenched samples the cT phase is stabilized below 90 K and at ambient pressure. Hence, the ambient-pressure 960° C quenched sample structure should roughly correspond to the structure of the Sn-grown sample at an intermediate pressure between ambient pressure and 0.63 GPa which is precisely what the Fe-As bond lengths in Fig. 9 a) show. The exception is a 50 K interval around the T-cT transition which is a consequence of hysteresis effects associated with the volume collapse. Since the collapsed phase is much stiffer than the tetragonal phase^{43,65,66} we expect reduction of the structural differences between the Sn-grown samples under pressure and the 960° C quenched samples, which is again confirmed by our data. Similar consistency in bond length values as well as jump at T_{cT} is observed in the behavior of interlayer As-As bonds, shown in Fig. 9 b).

However, the most striking feature observed in Fig. 9 a) is the reversal of Fe-As bond contraction in the cT phase and we believe that this is the key to understanding the mechanism behind the stabilization of cT phase at ambient pressure. Since, the formation of the cT phase is precipitated by the formation of interlayer As-As bonds, we need to look closer into the interplay of Fe-As and As-As bonding dynamics (Fig. 9 b)).

Examination of the behavior of the V_{zz} electric field gradient component for the iron and arsenic nuclei (Fig. 10) in the collapsed tetragonal phase in CaFe_2As_2 shows that each component follows a different trend. While the electric field gradient decreases at the iron nucleus, it increases at the arsenic nucleus as a consequence of the bonding behavior. Relative weakening of the Fe-As bond implies that charge density in the bonding region is reduced, leading to the reduction of the electric field gradient on the iron site. This is reflected in the angular momentum resolved electric field gradient tensor³⁹ which shows a major contributions coming from the $l = 1$ component, implicating reduced hybridization of iron $3d$ orbitals with arsenic $4p$ orbitals as a main culprit leading to the reduction of the electric field gradient. On the other hand, the increase of the electric field gradient at the arsenic site follows from the stronger interlayer As-As bonding as the sample is cooled. This is also reflected in the angular momentum resolved electric field gradient, with $l = 1$ component being essentially the only contribution. Such bond dynamics indicates that some of the charge in the Fe-As bond region is transferred to the interlayer As-As bond region, contributing to its strength and helping to stabilize the collapsed tetragonal phase at ambient pressure.

For further answers we examine in Fig. 9 b) the predicted interlayer As-As bond lengths for the 960°C quenched sample at ambient pressure. We again compare with the effect of the hydrostatic pressure and show the measured values for Sn-grown CaFe_2As_2 samples at the pressure of 0.63 GPa. We observe that the As-As bonds appear to be relatively longer in the tetragonal phase of the 960°C quenched sample. Such bond configuration can lead to charge saturation in the Fe-As bond region under thermal contraction, meaning that at a certain temperature it becomes energetically more favorable to transfer some of the charge into the relatively less charge dense interlayer As-As bond region, precipitating the formation of the interlayer As-As bond which in turn stabilizes the collapsed tetragonal phase. This process continues in the collapsed tetragonal phase, where the Fe-As bond keeps getting weaker while the interlayer As-As bond gets stronger until zero temperature is

reached, where the bond lengths revert to the ratio observed in the Sn-grown samples under hydrostatic pressure.

V. SUMMARY

Experimental clear features in the temperature dependencies of the isomer shift, relative spectral area and quadrupole splitting are observed at the transition from tetragonal to cT phase in CaFe_2As_2 . From the analysis of the temperature dependent isomer shift and spectral area data, as well as the temperature evolution of the intensity ratio, an average stiffening of the phonon modes in the cT phase is inferred. Quadrupole splitting increases by $\sim 25\%$ on cooling from room temperature to the cT transition, in agreement with a large anisotropy of thermal expansion in this temperature region. A clear unusual cusp was observed in the QS(T) data at the cT transition. The origin of it is not clear and requires additional studies.

Additionally, we performed *ab initio* density functional theory calculations of the electric field gradient and the electron density of CaFe_2As_2 in the tetragonal and collapsed tetragonal phase. Comparison of these calculations to the measurements allows for the determination of the As z -coordinates in the 960°C quenched sample, providing the full structural information under these conditions and allowing us to probe the microscopic origin of the experimental observations.

We have found that the resulting Fe-As bond lengths are consistent with the data recorded for Sn-grown samples under hydrostatic pressure, as expected from the broad similarity of the observed structural effects and proper accounting of differences in experimental conditions. In the tetragonal phase, as the sample is cooled, the Fe-As bonds undergo thermal contraction, resulting in larger electric field gradients at the iron nuclei and leading to an increase of the quadrupole splitting. In the collapsed tetragonal phase we observe instead an anomalous behavior of the Fe-As bond, whereby it undergoes expansion as the sample is cooled, resulting in a decrease of the observed quadrupole splitting. We attribute this behavior to charge redistribution from the Fe-As bond region into the interlayer As-As region, increasing the As-As bonding strength and resulting in stabilization of the collapsed tetragonal phase. In our proposed scenario, it is high temperature quenching at 960°C which stabilizes the relatively shorter Fe-As bonds, leading to charge saturation of the Fe-As bond

region as the sample contracts.

ACKNOWLEDGMENTS

X.M. was supported in part by the China Scholarship Council. Work at the Ames Laboratory was supported by the US Department of Energy, Basic Energy Sciences, Division of Materials Sciences and Engineering under Contract No. DE-AC02-07CH11358. M.T. and R.V. acknowledge financial support by the DFG (Deutsche Forschungsgemeinschaft) through grant SPP 1458.

* Currently at the Department of Physics, University of California - San Diego

- ¹ N. Ni, S. Nandi, A. Kreyssig, A. I. Goldman, E. D. Mun, S. L. Bud'ko, and P. C. Canfield, *Phys. Rev. B* **78**, 014523 (2008).
- ² A. I. Goldman, D. N. Argyriou, B. Ouladdiaf, T. Chatterji, A. Kreyssig, S. Nandi, N. Ni, S. L. Bud'ko, P. C. Canfield, and R. J. McQueeney, *Phys. Rev. B* **78**, 100506 (2008).
- ³ G. Wu, H. Chen, T. Wu, Y. L. Xie, Y. J. Yan, R. H. Liu, X. F. Wang, J. J. Ying, and X. H. Chen, *J. Phys. Condens. Matter* **20**, 422201 (2008).
- ⁴ F. Ronning, T. Klimczuk, E. D. Bauer, H. Volz, and J. D. Thompson, *J. Phys. Condens. Matter* **20**, 322201 (2008).
- ⁵ P. C. Canfield, S. L. Bud'ko, N. Ni, A. Kreyssig, A. I. Goldman, R. J. McQueeney, M. S. Torikachvili, D. N. Argyriou, G. Luke, and W. Yu, *Physica C* **469**, 404 (2009).
- ⁶ M. Alzamora, J. Munevar, E. Baggio-Saitovitch, S. L. Bud'ko, Ni Ni, P. C. Canfield, and D. R. Sánchez, *J. Phys. Condens. Matter* **23**, 145701 (2011).
- ⁷ Milton S. Torikachvili, Sergey L. Bud'ko, Ni Ni, and Paul C. Canfield, *Phys. Rev. Lett.* **101**, 057006 (2008).
- ⁸ A. Kreyssig, M. A. Green, Y. Lee, G. D. Samolyuk, P. Zajdel, J. W. Lynn, S. L. Bud'ko, M. S. Torikachvili, N. Ni, S. Nandi, J. B. Leão, S. J. Poulton, D. N. Argyriou, B. N. Harmon, R. J. McQueeney, P. C. Canfield, and A. I. Goldman, *Phys. Rev. B* **78**, 184517 (2008).
- ⁹ A. I. Goldman, A. Kreyssig, K. Prokeš, D. K. Pratt, D. N. Argyriou, J. W. Lynn, S. Nandi, S. A. J. Kimber, Y. Chen, Y. B. Lee, G. Samolyuk, J. B. Leão, S. J. Poulton, S. L. Bud'ko, N. Ni,

- P. C. Canfield, B. N. Harmon, and R. J. McQueeney, Phys. Rev. B **79**, 024513 (2009).
- ¹⁰ W. Yu, A. A. Aczel, T. J. Williams, S. L. Bud'ko, N. Ni, P. C. Canfield, and G. M. Luke, Phys. Rev. B **79**, 020511 (2009).
- ¹¹ Hanoh Lee, Eunsung Park, Tuson Park, V. A. Sidorov, F. Ronning, and E. D. Bauer, and J. D. Thompson, Phys. Rev. B **80**, 024519 (2009).
- ¹² Sergey L. Bud'ko, Ni Ni, and Paul C. Canfield, Philos. Mag. **90**, 1219 (2010).
- ¹³ M. S. Torikachvili, S. L. Bud'ko, N. Ni, P. C. Canfield, and S. T. Hannahs, Phys. Rev. B **80**, 014521 (2009).
- ¹⁴ K. Prokes, A. Kreyssig, B. Ouladdiaf, D. K. Pratt, N. Ni, S. L. Bud'ko, P. C. Canfield, R. J. McQueeney, D. N. Argyriou, and A. I. Goldman, Phys. Rev. B **81**, 180506 (2010).
- ¹⁵ S. Ran, S. L. Bud'ko, D. K. Pratt, A. Kreyssig, M. G. Kim, M. J. Kramer, D. H. Ryan, W. N. Rowan-Weetaluktuk, Y. Furukawa, B. Roy, A. I. Goldman, and P. C. Canfield, Phys. Rev. B **83**, 144517 (2011).
- ¹⁶ S. Ran, S. L. Bud'ko, W. E. Straszheim, J. Soh, M. G. Kim, A. Kreyssig, A. I. Goldman, and P. C. Canfield, Phys. Rev. B **85**, 224528 (2012).
- ¹⁷ S. Ran, S. L. Bud'ko, W. E. Straszheim, and P. C. Canfield, Phys. Rev. B **90**, 054501 (2014).
- ¹⁸ E. Gati, S. Köhler, D. Guterding, B. Wolf, S. Knöner, S. Ran, S. L. Bud'ko, P. C. Canfield, and M. Lang, Phys. Rev. B **86**, 220511 (2012).
- ¹⁹ J. H. Soh, G. S. Tucker, D. K. Pratt, D. L. Abernathy, M. B. Stone, S. Ran, S. L. Bud'ko, P. C. Canfield, A. Kreyssig, R. J. McQueeney, and A. I. Goldman, Phys. Rev. Lett. **111**, 227002 (2013).
- ²⁰ Y. Furukawa, B. Roy, S. Ran, S. L. Bud'ko, and P. C. Canfield, Phys. Rev. B **89**, 121109 (2014).
- ²¹ Sergey L. Bud'ko, Sheng Ran, and Paul C. Canfield, Phys. Rev. B **88**, 064513 (2013).
- ²² R. S. Dhaka, Rui Jiang, S. Ran, S. L. Bud'ko, P. C. Canfield, B. N. Harmon, Adam Kaminski, Milan Tomić, Roser Valení, and Yongbin Lee, Phys. Rev. B **89**, 020511 (2014).
- ²³ K. Gofryk, B. Saparov, T. Durakiewicz, A. Chikina, S. Danzenbächer, D. V. Vyalikh, M. J. Graf, and A. S. Sefat, Phys. Rev. Lett. **112**, 186401 (2014).
- ²⁴ Bayrammurad Saparov, Claudia Cantoni, Minghu Pan, Thomas C. Hogan, William Ratcliff II, Stephen D. Wilson, Katharina Fritsch, Bruce D. Gaulin, and Athena S. Sefat Sci. Rep. **4**, 4120 (2014).
- ²⁵ Marianne Rotter, Marcus Tegel, Dirk Johrendt, Inga Schellenberg, Wilfried Hermes, and Rainer

- Pöttgen, Phys. Rev. B **78**, 020503 (2008).
- ²⁶ Israel Nowik, Israel Felner, Physica C **469**, 485 (2009).
- ²⁷ I. Nowik, I. Felner, Z. Ren, Z. A. Xu, and G. H. Cao, J. Phys.: Conf. Ser. **217**, 012121 (2010).
- ²⁸ Amar Nath and Airat Khasanov, in: *Mossbauer Spectroscopy: Applications in Chemistry, Biology, and Nanotechnology*, edited by Virender K. Sharma, Gostar Klingelhofer, and Tetsuaki Nishida, John Wiley & Sons, Inc. (2013) p. 535.
- ²⁹ A. K. Jasek, K. Komędera, A. Błachowski, K. Ruebenbauer, J. Żukrowski, Z. Bukowski, and J. Karpinski, Philos. Mag. **95**, 493 (2015).
- ³⁰ Neeraj Kumar, R. Nagalakshmi, R. Kulkarni, P. L. Paulose, A. K. Nigam, S. K. Dhar, and A. Thamizhavel, Phys. Rev. B **79**, 012504 (2009).
- ³¹ Zhiwei Li, Xiaoming Ma, Hua Pang, and Fashen Li, J. Phys. Condens. Matter **23**, 255701 (2011).
- ³² A. Błachowski, K. Ruebenbauer, J. Żukrowski, K. Rogacki, Z. Bukowski, and J. Karpinski, Phys. Rev. B **83**, 134410 (2011).
- ³³ Xiaoming Ma, Sheng Ran, Paul C. Canfield, Sergey L. Bud'ko, J. Alloys Compd **657**, 379 (2016).
- ³⁴ Yui Sakaguchi, Shugo Ikeda, Tetsuji Kuse and Hisao Kobayashi, J. Phys. Condens. Matter **26**, 295702 (2014).
- ³⁵ Sheng Ran, *Combined effects of post-growth thermal treatment and chemical substitution on physical properties of CaFe₂As₂*, Ph. D. Thesis, Iowa State Universty (2014).
- ³⁶ Philipp Gütlich, Eckhard Bill, and Alfred X. Trautwein, *Mössbauer Spectroscopy and Transition Metal Chemistry. Fundamentals and Applications*, Springer-Verlag, Berlin, Heidelberg, (2011).
- ³⁷ Z. Klencsár, MossWinn 3.0i xp Manual (1995-2009).
- ³⁸ K. Koepernik and H. Eschrig, Phys. Rev. B **59**, 1743 (1999).
- ³⁹ K. Koch, K. Koepernik, D. V. Neck, H. Rosner and S. Cottenier, Phys. Rev. B **81** 032507 (2010).
- ⁴⁰ J. P. Perdew, K. Burke and M. Ernzerhof, Phys. Rev. Lett. **77**, 3865 (1996).
- ⁴¹ P. Blaha, K. Schwarz, G. K. H. Madsen, D. Kvasnicka, and J. Luitz, An Augmented Plane Wave Plus Local Orbitals Program for Calculating Crystal Properties (Karlheinz Schwarz, Techn. Universität Wien, Austria) (2001).
- ⁴² N.N. Greenwood and T.C. Gibb., *Mössbauer Spectroscopy*, (Chapman and Hall Ltd, London)

- (1971)
- ⁴³ R. Mittal, S. K. Mishra, S. L. Chaplot, S. V. Ovsyannikov, E. Greenberg, D. M. Trots, L. Dubrovinsky, Y. Su, Th. Brueckel, S. Matsuishi, H. Hosono, and G. Garbarino, *Phys. Rev. B* **83**, 054503 (2011).
- ⁴⁴ R. Mittal, R. Heid, A. Bosak, T. R. Forrest, S. L. Chaplot, D. Lamago, D. Reznik, K.-P. Bohnen, Y. Su, N. Kumar, S. K. Dhar, A. Thamizhavel, Ch. Rüegg, M. Krisch, D. F. McMorrow, Th. Brueckel, and L. Pintschovius, *Phys. Rev. B* **81**, 144502 (2010).
- ⁴⁵ O. Eriksson and A. Svane, *J. Phys.: Cond. Mat.* **1**, 1589 (1989).
- ⁴⁶ T. Lovell, W.-G. Han, T. Liu and L. Noodleman, *J. Am. Chem. Soc.* **124** 5890 (2002)
- ⁴⁷ F. Neese, *Inorg. Chim. Acta* **337**, 181 (2002)
- ⁴⁸ S. Sinnecker, L. D. Slep, E. Bill and F. Neese, *Inorg. Chem.* **44**, 2245 (2005)
- ⁴⁹ W.-G. Han, T. Liu and T. Lovell, *J. Comput. Chem.* **27**, 1292 (2006)
- ⁵⁰ R. Hoffmann, C. Zheng, *J. Phys. Chem.* **89**, 4175 (1985)
- ⁵¹ G. R. Stewart, *Rev. Mod. Phys.* **83**, 1589 (2011).
- ⁵² S. Lauer, V. R. Marathe and A. Trautwein, *Phys. Rev. A* **19**, 1852 (1979)
- ⁵³ P. Dufek, P. Blaha and K. Schwarz, *Phys. Rev. Lett.* **75**, 3545 (1995)
- ⁵⁴ G. Martínez-Pinedo, P. Schwerdtfeger, E. Caurier, K. Langanke, W. Nazarewicz and T. Söhnel, *Phys. Rev. Lett.* **87**, 062701 (2001)
- ⁵⁵ Y. Zhang, W. Gossman and E. Oldfield, *J. Am. Chem. Soc.* **125**, 16387 (2003)
- ⁵⁶ Y. Zhang and E. Oldfield, *J. Phys. Chem.* **107**, 4147 (2003)
- ⁵⁷ Z. Zhi, D. Guenzburger and D. E. Ellis, *J. Theo. Chem.* **678**, 145 (2004)
- ⁵⁸ Jean Diehl, Steffen Backes, Daniel Guterding, Harald O. Jeschke, and Roser Valentí, *Phys. Rev. B* **90**, 085110 (2014)
- ⁵⁹ Subhasish Mandal, R. E. Cohen, and K. Haule, *Phys. Rev. B* **90**, 060501(R) (2014)
- ⁶⁰ D. K. Pratt, Y. Zhao, S. A. J. Kimber, A. Hiess, D. N. Argyriou, C. Broholm, A. Kreyssig, S. Nandi, S. L. Bud'ko, N. Ni, P. C. Canfield, R. J. McQueeney, and A. I. Goldman, *Phys. Rev. B* **79**, 060510(R) (2009)
- ⁶¹ Z. P. Yin, S. Lebégue, M. J. Han, B. P. Neal, S. Y. Savrasov, and W. E. Pickett, *Phys. Rev. Lett.* **101**, 047001 (2008)
- ⁶² I. I. Mazin, M. D. Johannes, L. Boeri, K. Koepf, and D. J. Singh, *Phys. Rev. B* **78**, 085104 (2008)

- ⁶³ I. Opahle, H. C. Kandpal, Y. Zhang, C. Gros, R. Valentí, Phys. Rev. B **79**, 024509 (2009).
- ⁶⁴ M. Aichhorn, L. Pourovskii, and A. Georges, Phys. Rev. B **84**, 054529 (2011)
- ⁶⁵ M. Tomić, R. Valentí and H. O. Jeschke, Phys. Rev. B **85**, 094105 (2012).
- ⁶⁶ T. Yildirim, Phys. Rev. Lett. **102**, 037003 (2009)

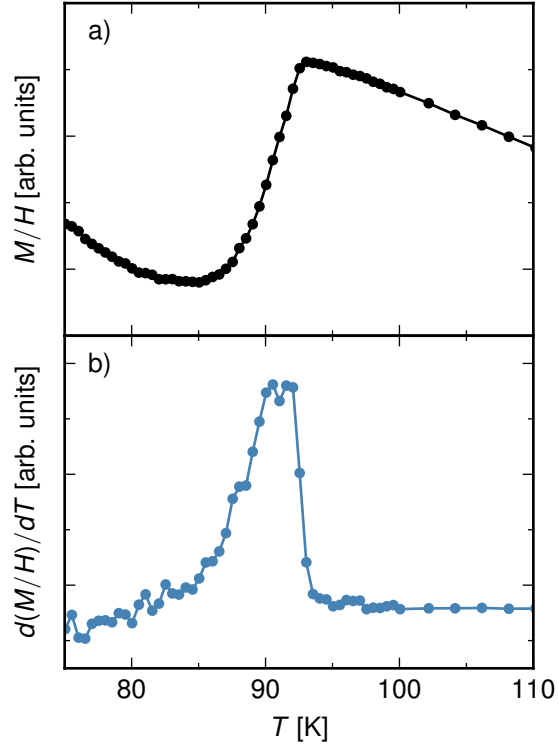


FIG. 1. Temperature dependent magnetization, $M/H(T)$ and its temperature derivative, $d(M/H)/dT$, of a part of CaFe_2As_2 crystals mosaic used for Mössbauer measurements in the vicinity of the cT transition. Note that the paper and adhesive of the mount give some small, weakly temperature dependent contribution to $M/H(T)$.

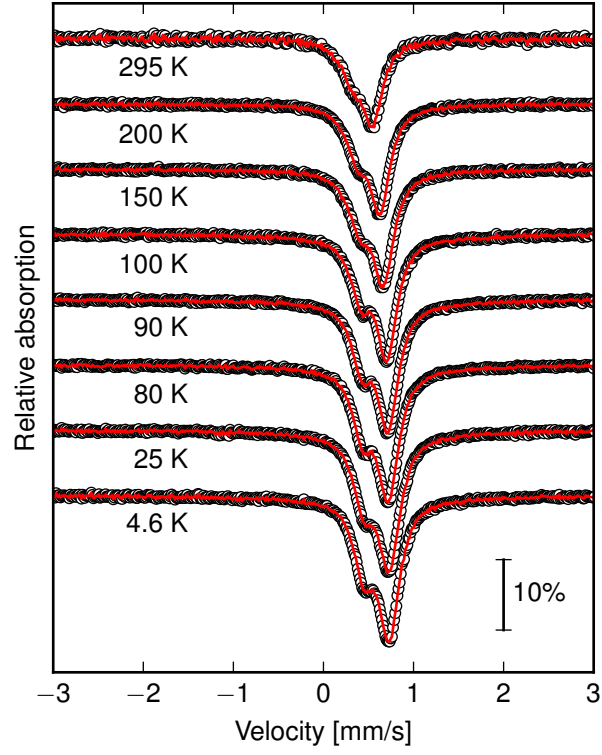


FIG. 2. (Color online) ^{57}Fe Mössbauer spectra of CaFe_2As_2 at selected temperatures. Symbols - data, lines - fits. $T_{cT} \sim 90$ K, as shown in Fig. 1.

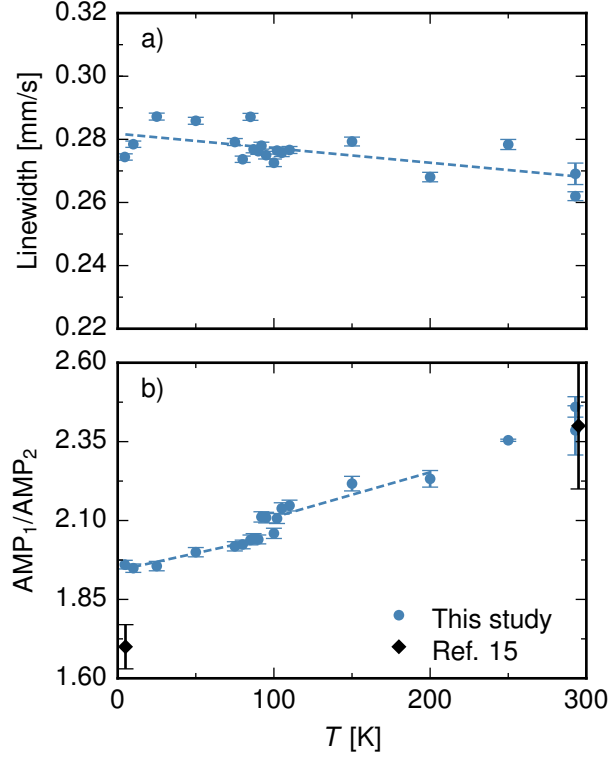


FIG. 3. (Color online) CaFe_2As_2 ^{57}Fe Mössbauer data: (a) Temperature dependence of the linewidth; (b) The intensity ratio of the doublet lines as a function of temperature. Circles - this work, rhombuses - Ref. 15. Dashed lines are linear fit to the data [panel a)] and guides to the eye [panel b)].

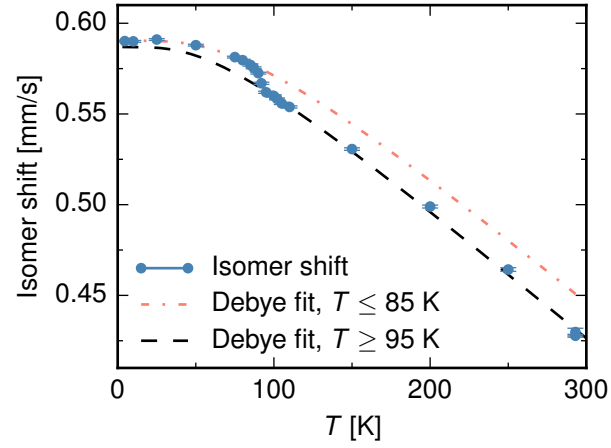


FIG. 4. (Color online) Temperature dependent isomer shift of CaFe_2As_2 . Dashed line - Debye fit for $T \geq 95$ K resulting in $\Theta_D = 239 \pm 16$ K, dash-dotted line Debye fit for $T \leq 85$ K resulting in $\Theta_D = 316 \pm 7$ K

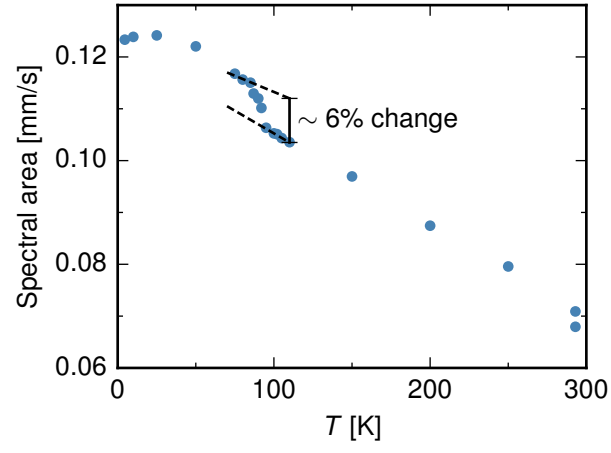


FIG. 5. (Color online) Temperature dependent relative spectral area of CaFe₂As₂. Dashed lines are guides to the eye. 6% change is shown as a vertical bar.

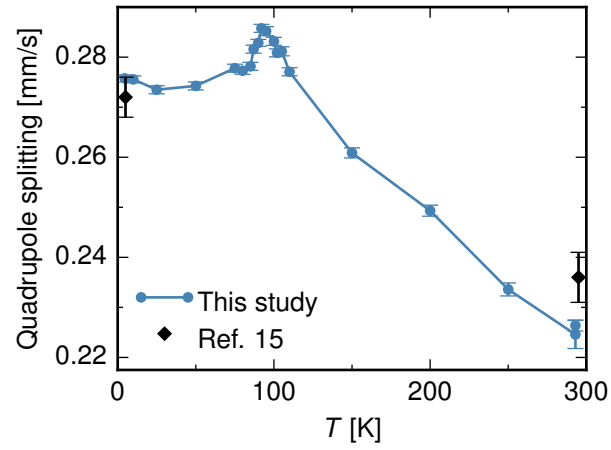


FIG. 6. (Color online) Temperature dependent quadrupole splitting of CaFe₂As₂. Circles - this work, rhombuses - Ref. 15.

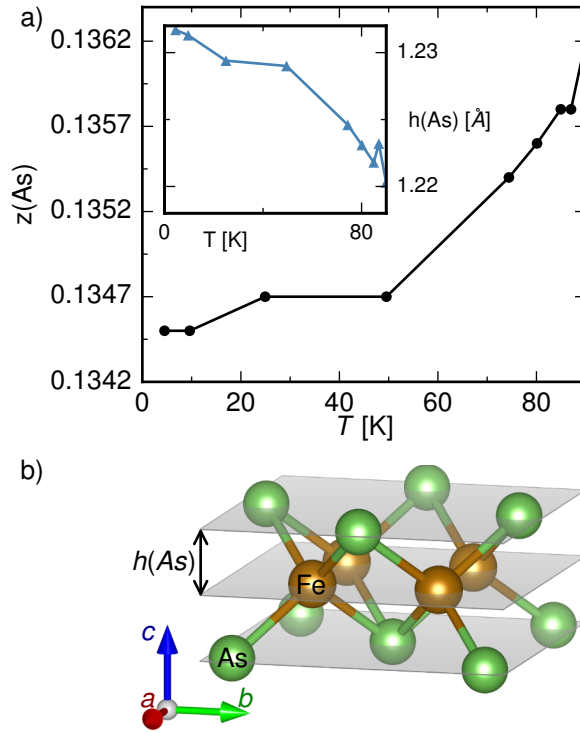


FIG. 7. (Color online) (a) Calculated temperature dependence of As z -coordinate in the collapsed-tetragonal phase. The inset shows temperature dependence of height of As atoms above the Fe plane. (b) Diagram showing geometry of the FeAs layer.

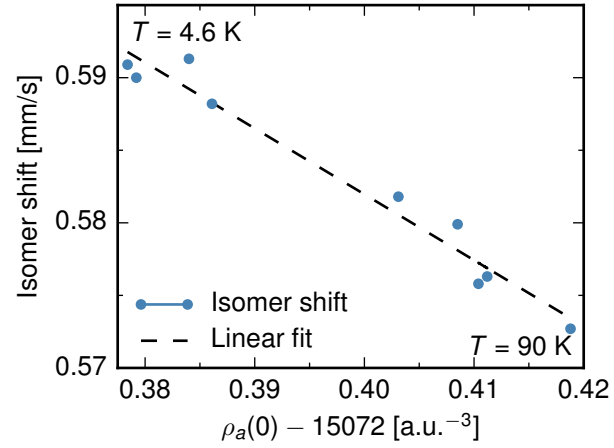


FIG. 8. (Color online) The linear relationship between the calculated charge density at the iron nucleus and the measured isomer shift in the collapsed-tetragonal phase. Note: implicit temperature variation is shown by temperature values for the end points.

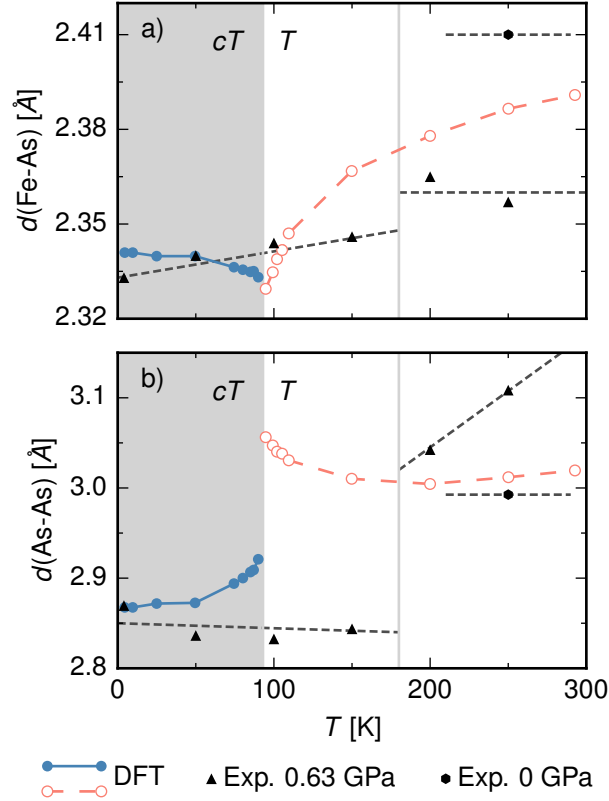


FIG. 9. (Color online) (a) The *ab-initio* predicted Fe-As bond length in the 960° C quenched sample compared against the measured bond lengths on Sn-grown samples under hydrostatic pressure⁸. Dotted lines are guides for the eye. (b) Predicted interlayer As-As bond lengths in the 960° C quenched sample compared against the Sn-grown samples⁸. Vertical line marks T_{cT} at $P = 0.63$ GPa. Please note that the comparison to experimental data is intended to estimate the properties of the “intrinsic” pressure in 960° C quenched sample (see the text for details).

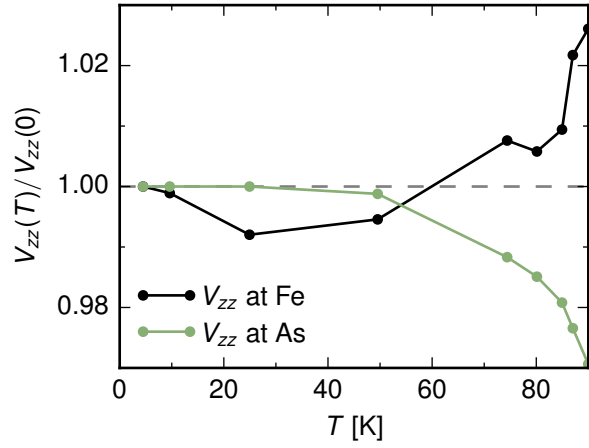


FIG. 10. (Color online) The calculated V_{zz} component of the electric field gradient for the iron and arsenic sites normalized to their respective zero temperature values.